

CONTENTS

1	NARROW LINE REGION PROPERTIES	1
1.1	Introduction	1
1.2	Quasar Sample	2
1.3	Parametric model fits	2
1.3.1	Redshift transformation	3
1.3.2	Removal of Fe II emission	4
1.3.3	Modelling H β /[O III]	4
1.3.4	Deriving upper limits on the [O III] EQW	7
1.3.5	Modelling H α	8
1.3.6	Derived parameters	8
1.3.7	Deriving uncertainties on parameters	12
1.3.8	Low EQW [O III]	12
1.3.9	Reliability of redshift estimates	12
1.4	Results	13
1.4.1	Luminosity/redshift-evolution of [O III] properties	16
1.4.2	Velocity width	19
1.4.3	Eigenvector 1 correlations	19
1.4.4	[O III] and C IV outflows are linked	22
1.5	Discussion	27
1.6	ICA	27
1.6.1	Model Two: Independent Component Analysis	28
1.6.2	Physical interpretation of ICA components	29
1.6.3	ICA fits	32

LIST OF FIGURES

Figure 1.1	Spectra of the 24 objects for which significant Fe II emission is still visible following our Fe II-subtraction procedure. 5
Figure 1.1	Continued. 6
Figure 1.2	Model fits to the continuum- and Fe II-subtracted H β /[O III] emission in 15 quasars, chosen at random. 9
Figure 1.3	Uncertainty in v_{10} as a function of the EQW, for [O III]. 13
Figure 1.4	Comparison of systemic redshift estimates using [O III], broad H β and broad H α . 14
Figure 1.5	Correlations between the line width w_{80} , asymmetry R and EQW of [O III]. 15
Figure 1.6	The [O III] EQW as a function of the quasar bolometric luminosity for the sample presented in this chapter (blue circles) and the low- z SDSS sample (grey points and contours). 17
Figure 1.7	The [O III] velocity-width, characterised by w_{80} , as a function the [O III] luminosity and the quasar redshift. 18
Figure 1.8	EV1 parameter space. 20
Figure 1.9	[O III] EQW as a function of the C IV blueshift. 21
Figure 1.10	The high-redshift EV1 parameter space of C IV blueshift and EQW. 23
Figure 1.11	Model fits to the continuum- and Fe II-subtracted H β /[O III] emission in 18 quasars with extreme [O III] emission profiles. 24
Figure 1.13	The relation between the blueshifts of C IV and [O III]. 26
Figure 1.14	H β /[O III] emission J002952+020607. The ICA reconstruction is shown in black, and the spectrum in grey. The first three components, and the sum of components four, five and six are shown individually. 30
Figure 1.15	[O III] emission in J002952+020607. 31
Figure 1.16	The relative weight in each of the six positive ICA components for the high-luminosity and low luminosity samples. 33

Figure 1.17	The relative weight in the three ICA components corresponding to [O III] emission and the relative weight of the component most closely related to blueshifted [O III] emission relative to all three [O III] components. 34
Figure 1.18	Weight in the [O III] wing relative to the weight in the [O III] core emission versus the strength of the core [O III] emission. 34
Figure 1.19	The ICA component weight w_4 , which is a proxy for the strength of core [O III], as a function of the C IV blueshift. 35
Figure 1.20	Median ICA-reconstructed spectra as a function of the C IV blueshift. 35

LIST OF TABLES

Table 1.1	The numbers of quasars with [O III] line measurements and the spectrographs and telescopes used to obtain the near-infrared spectra. 3
Table 1.2	Summary of models used to fit the H α emission, and the number of quasars each model is applied to. 8
Table 1.3	The format of the table containing the emission line properties from our parametric model fits. 10
Table 1.4	Physical interpretation of the ICA components. 30

LISTINGS

ACRONYMS

AGN Active Galactic Nuclei

NLR Narrow Line Region

BLR Broad Line Region

EV₁ Eigenvector 1

ICA Independent Component Analysis

PCA Principal Component Analysis

SDSS Sloan Digital Sky Survey

BOSS Baryon Oscillation Spectroscopic Survey

UV Ultra-Violet

EQW Equivalent Qidth

S/N Signal-to-noise

BH Black Hole

SED Spectral Energy Distribution

IR Infrared

NIR Near-infrared

FWHM Full-Width-at-Half-Maximum

NARROW LINE REGION PROPERTIES

1.1 INTRODUCTION

X-ray and UV spectroscopy has revealed high velocity outflows to be nearly ubiquitous in high accretion rate AGN. Models of galaxy evolution that invoke AGN feedback require these outflows to reach galactic scales and quench star formation in the AGN host galaxies. In recent years, a huge amount of resources have been devoted to searching for observational evidence of these galaxy-wide, AGN-driven outflows. This has resulted in recent detections of outflows in AGN-host galaxies using tracers of atomic, molecular, and ionised gas (e.g. Nesvadba et al., 2006; Arav et al., 2008; Nesvadba et al., 2008; Moe et al., 2009; Dunn et al., 2010; Alexander et al., 2010; Harrison et al., 2012; Harrison et al., 2014; Nesvadba et al., 2010; Rupke and Veilleux, 2013; Veilleux et al., 2013; Nardini et al., 2015; Feruglio et al., 2010; Alatalo et al., 2011; Cimatti et al., 2013; Ciccone et al., 2014).

One particularly successful technique has been observing forbidden emission lines, which trace warm ($T \sim 10^4 K$) ionised gas in the AGN NLR. Because of its high equivalent width, $[O\text{ III}]\lambda 5008$ is the most studied of the narrow AGN emission lines. In general, the $[O\text{ III}]$ emission consists of two distinct components: a narrow, ‘core’ component, with a velocity close to the systemic redshift of the host galaxy, and a broader ‘wing’ component, which is normally blueshifted. The general consensus is that the core component traces the gravitational potential of the host galaxy, as the width correlates well with the stellar velocity dispersion. On the other hand, the broad, blueshifted wing is tracing outflowing gas. This emission appears blueshifted because the far-side of the outflow - that is, the side which is moving away from the line of sight - is obscured (e.g. Heckman et al., 1981; Vrtilek, 1985).

Observations of broad velocity-widths and blueshifts in narrow emission lines stretch back several decades (e.g. Weedman, 1970; Stockton, 1976; Heckman et al., 1981; Veron, 1981; Feldman et al., 1982; Heckman, Miley, and Green, 1984; Vrtilek, 1985; Whittle, 1985; Boroson and Green, 1992). However, these studies rely on small samples, which are often unrepresentative of the properties of the population. More recently, the advent of large optical spectroscopic surveys (e.g. SDSS) have facilitated studies of the NLR in tens of thousands of AGN (e.g. Boroson, 2005; Greene and Ho, 2005; Zhang et al., 2011; Mullaney et al., 2013; Zakamska and Greene, 2014; Shen and Ho, 2014). This has provided constraints on the prevalence and drivers

of ionised outflows. At the same time, there is strong evidence from spatially resolved spectroscopic observations that these outflows are extended over galaxy scales (e.g. Greene et al., 2009; Greene et al., 2011; Hainline et al., 2013; Harrison et al., 2012; Harrison et al., 2014).

However, these studies do not cover the redshift range when star formation and BH accretion peaked, and consequently when feedback is predicted to be strongest. At these redshifts the bright optical emission lines are redshifted to near-infrared wavelengths, where observations are much more challenging. As a consequence, studies at high redshifts have typically relied on relatively small numbers of objects (e.g. Netzer et al., 2004; Sulentic et al., 2004; Shen, 2016). These studies find [O III] to be broader in more luminous AGN, suggesting that AGN efficiency in driving galaxy-wide outflows increases with luminosity (e.g. Netzer et al., 2004; Nesvadba et al., 2008; Kim et al., 2013; Brusa et al., 2015; Carniani et al., 2015; Perna et al., 2015; Bischetti et al., 2016). The fraction of objects with very weak [O III] emission also appears to increase with redshift and/or luminosity (e.g. Netzer et al., 2004).

Other recent studies have looked at the [O III] emission properties of extreme objects - e.g. heavily obscured quasars (Zakamska et al., 2016) and the most luminous quasars (Bischetti et al., 2016) - at redshifts $z \sim 2$. The [O III] emission in these objects is extremely broad and strongly blueshifted. These observations are consistent with galaxy formation models that predict AGN feedback to be strongest in luminous, dust-obscured quasars.

In this chapter we analyse the [O III] properties of a sample of 354 high-luminosity, redshift $1.5 < z < 4$ quasars. This is the largest study of the NLR properties of high redshift quasars ever undertaken.

1.2 QUASAR SAMPLE

From our near-infrared spectroscopic catalogue (Chapter ??), we have selected 354 quasars which have spectra covering the strong, narrow [O III] doublet. The broad Balmer H β line is also observed for all but two of the sample. In 165, the spectra extend to the broad H α emission line at 6565Å, and in 260 optical spectra including C IV are also available (mostly from SDSS/BOSS). The sample covers a wide range in redshifts ($1.5 \lesssim z \lesssim 4$) and luminosities ($45.5 \lesssim \log L_{\text{Bol}} \lesssim 49 \text{ erg s}^{-1}$). The spectrographs and telescopes used to obtain the near-infrared spectra are summarised in Table 1.1.

1.3 PARAMETRIC MODEL FITS

In this section, we describe how parameters of the [O III] emission are derived. Our approach is to model the spectra using a power-law continuum, an empirical Fe II template and multiple Gaussian compo-

Table 1.1: The numbers of quasars with [O III] line measurements and the spectrographs and telescopes used to obtain the near-infrared spectra.

Spectrograph	Telescope	Number
FIRE	MAGELLAN	31
GNIRS	GEMINI-N	28
ISAAC	VLT	7
LIRIS	WHT	7
NIRI	GEMINI-N	29
NIRSPEC	Keck II	3
SINFONI	VLT	80
SOFI	NTT	76
TRIPLESPEC	ARC-3.5m	27
TRIPLESPEC	P200	45
XSHOOTER	VLT	21
Total		354

nents to model the emission from the broad and narrow components of $H\beta$ and the [O III] doublet. Non-parametric emission line properties are then derived from the best-fitting model. This approach, which is commonly adopted in the literature (e.g. Shen et al., 2011; Shen and Liu, 2012; Shen, 2016), is more robust when analysing spectra with limited S/N (in comparison to measuring line properties directly from the data) and allows different emission lines to be de-blended.

The same approach was used to model the $H\beta$ /[O III] complex in Chapter ?? . However, a number of small adjustments have been made to the model (Section 1.3.3). $H\alpha$ emission line properties (used in this Chapter to estimate the quasar systemic redshift) are also re-derived using a slightly modified model (Section 1.3.5). C IV emission line properties (used to infer the strength of BLR outflows) are taken directly from Chapter ?? .

1.3.1 Redshift transformation

Before a spectrum can be modelled, it must first be transformed to the quasar rest-frame. The redshift used in this transformation is either derived from the peak of the broad $H\alpha$ emission (~ 40 per cent of our sample), from the peak of the broad $H\beta$ emission (~ 40 per cent) or from the peak of the narrow [O III] emission (20 per cent). The rest-frame transformation is only required to be accurate to within $\sim 1000 \text{ km s}^{-1}$ for our fitting procedure to work. In later sections, more

precise estimates of the systemic redshift will be calculated using our parametric model fits.

1.3.2 *Removal of Fe II emission*

Fe II emission is generally strong in the vicinity of $H\beta/[O III]$. Therefore, before $H\beta/[O III]$ is modelled, we first model and subtract the continuum and Fe II emission using the procedure described in Chapter ??.

We encountered 24 objects for which Fe II emission appears to be present in the spectrum even after the subtraction procedure (Figure ??). In these objects the relative strengths of the Fe II lines differ significantly from those of I Zw 1, on which the Fe II template we use is based. The residual Fe II emission is at rest-frame wavelengths very close to zero-velocity wavelengths of the [O III] doublet, which is generally very weak in these objects. The Gaussians we fit to the spectra to model [O III] are therefore strongly biased, and the [O III] emission properties we infer from the model are in error by large factors.

For example, J223819-092106 was analysed by Shen, (2016) using a very similar model. Shen, (2016) reported the [O III] emission in this object to be shifted by $\sim 7500 \text{ km s}^{-1}$ relative to the Hewett and Wild, (2010) systemic redshift. Our analysis suggests that emission which was modelled by Shen, (2016) as [O III] is more likely to be [poorly-subtracted Fe II emission]. Because the derived [O III] emission properties can be strongly biased in objects so-affected, these objects are flagged and are excluded from our analysis in the remainder of this chapter.

1.3.3 *Modelling $H\beta/[O III]$*

The $H\beta$ and [O III] emission is fit using the procedure described in Chapter ?. However, we make a number of modifications to the parametric model employed in the fit. The model employed in this Chapter is described in detail below.

In general, $H\beta$ is modelled by two Gaussians with non-negative amplitudes and FWHM greater than 1200 km s^{-1} . In 10 objects $H\beta$ is modelled with a single Gaussian and in 41 objects $H\beta$ is modelled with two Gaussians, but the velocity centroids of the two Gaussians are constrained to be equal. These spectra generally have low S/N, and adding extra freedom to the model does not significantly decrease the reduced χ^2 . In addition there are cases where the blue wing of the $H\beta$ emission is below the lower wavelength limit of the spectrograph; in these cases models with more freedom are insufficiently constrained by the data.

Contributions to the $H\beta$ emission from the NLR is weak in the vast majority of our sample, and in general we do not include an

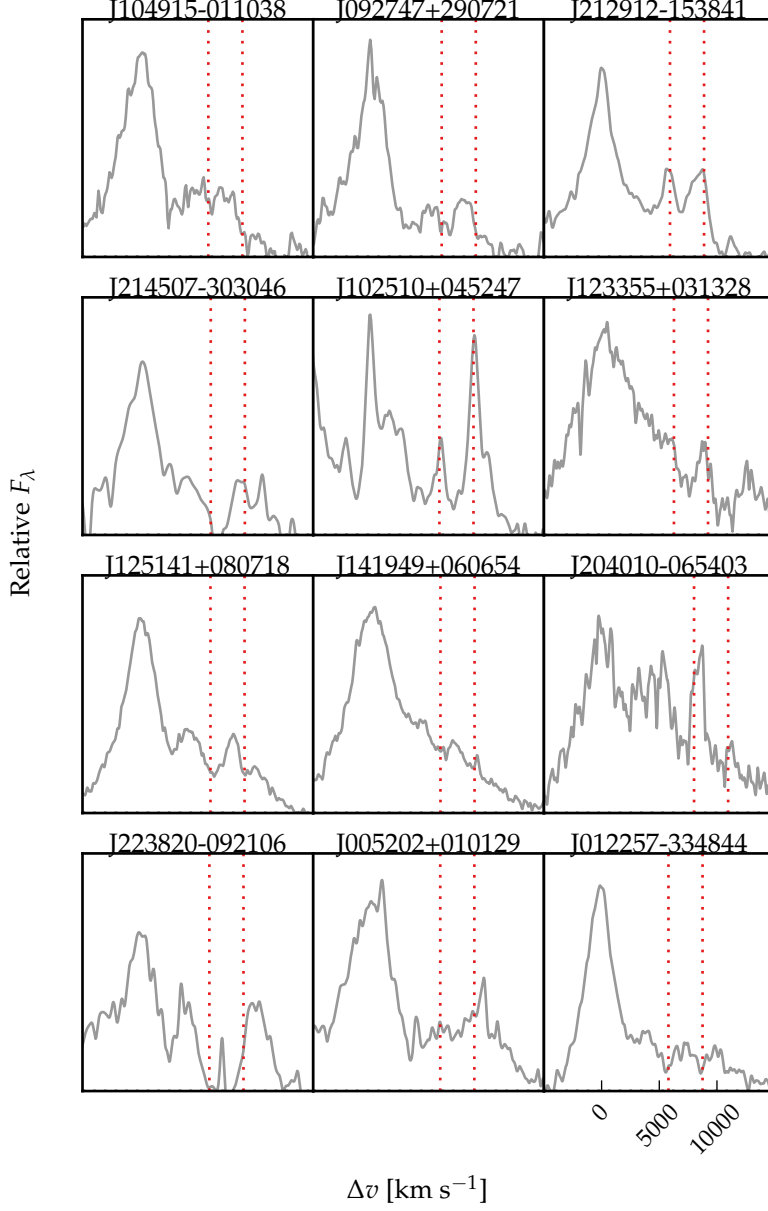


Figure 1.1: Spectra of the 24 objects for which significant Fe II emission is still visible following our Fe II-subtraction procedure. Spectra have been smoothed via convolution with a 100km s^{-1} Gaussian kernel. The vertical lines indicate the expected positions of the [O III] doublet (which is generally very weak) with the systemic redshift defined using the peak of the broad H β emission.

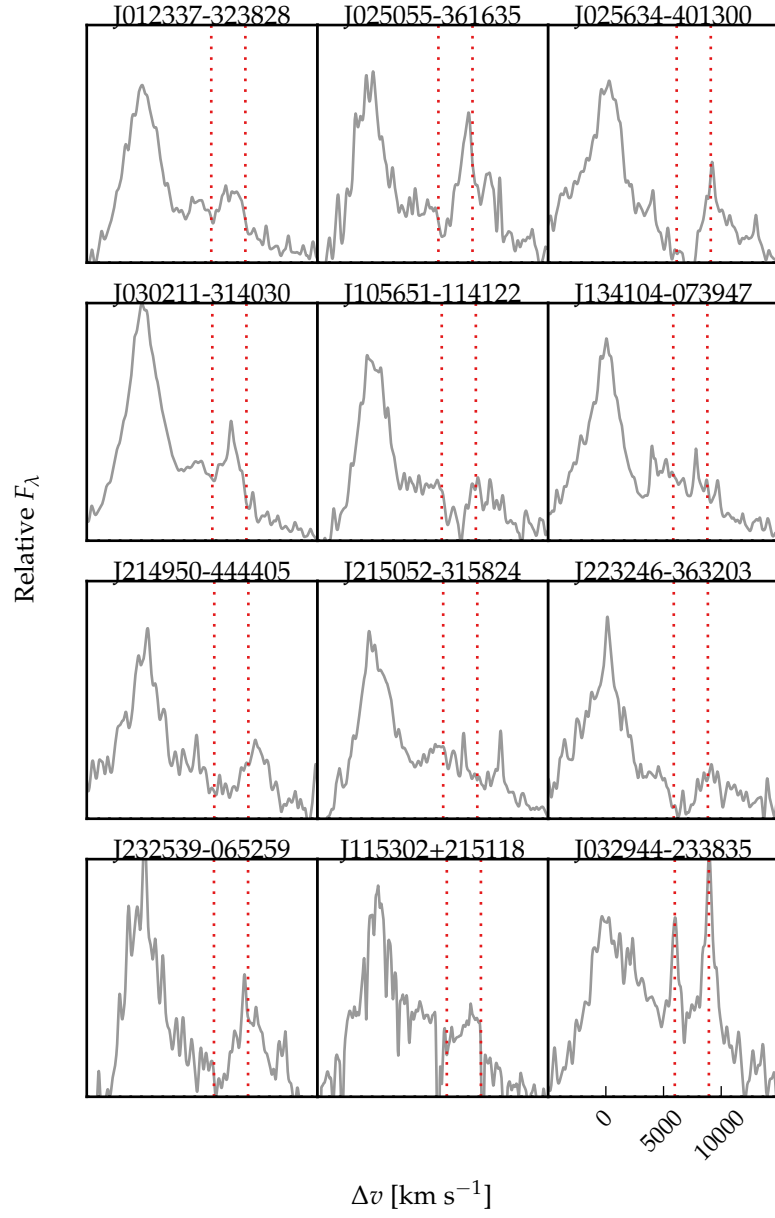


Figure 1.1: Continued.

additional Gaussian component to model this emission. In 9 objects features in the model - data residuals suggest that a narrow emission component is significant, and an additional narrow Gaussian is included for these quasars. It is likely that there is some not insignificant contribution from the NLR in other quasars in our sample. If this is the case then measures of the H β velocity width will be biased to lower values on average. However, measurements of the [O III] emission (the focus of this chapter) will not be affected by not decomposing H β into distinct broad and narrow components.

Each component of the [O III] doublet is fit with one or two Gaussians, depending on the fractional reduced χ^2 difference between the one- and two-component models. Concretely, if the addition of the second Gaussian decreases the reduced χ^2 by more than 5 per cent then the double-Gaussian model is accepted. One hundred and twenty-eight are fit with a single Gaussian and 140 with two Gaussians. The peak flux ratio of the [O III] 4960 Å and 5008 Å components are fixed at the expected 1:3 ratio and the width and velocity offsets are set to be equal¹.

In 62 objects with very weak [O III] (mean EQW ~ 2 Å) we found that the Gaussian model has a tendency to fit features of the noise. In some cases this can lead to large errors on the [O III] line properties. To avoid this problem, we instead fit a fixed [O III] template to the spectra, with the overall scaling the only free-parameter in the fit. This template is generated by running our line-fitting routine on a median composite spectrum of the 268 quasars with [O III] line measurements. The spectra used to construct the composite were first de-redshifted and continuum- and Fe II-subtracted.

In Figure 1.2 we show example fits to 15 objects, chosen at random. The mean reduced chi-squared value is 1.74 and, in general, there are no strong features observable in the spectrum minus model residuals.

1.3.4 Deriving upper limits on the [O III] EQW

Firstly, the best-fitting model comprising the continuum, Fe II, and H β emission is subtracted from the spectra, leaving behind only emission due to [O III]. These spectra are then smoothed by convolving with a Gaussian of width 200 km s^{-1} . From each of these spectra we generate 100 mock spectra, with the flux at each wavelength randomly drawn from a Normal distribution with a mean equal to the smoothed flux and a width equal to the error on the flux. We then perform an error-weighted linear least-squares regression with the [O III] template described in the preceding section. The EQW and its error are then defined as the mean and root-mean-square error of the

¹ For QSO176, a significantly better fit ($\Delta\chi^2_{\nu} \sim 25\%$) is obtained when the peak flux ratio constraint relaxed; the peak ratio of the best-fitting model is 0.47.

Table 1.2: Summary of models used to fit the H α emission, and the number of quasars each model is applied to.

Model	Components	Fix centroids?	Number
1	1 broad Gaussian	N/A	10
2	2 broad Gaussians	Yes	71
3	2 broad Gaussians	No	32
4	2 broad Gaussians + narrow Gaussians	Yes	51
5	2 broad Gaussians + narrow Gaussians	No	53

best-fitting EQW in the 100 realisations. We define the upper limit on the [O III] EQW as the mean plus the error.

*Paul: does this way
of deriving upper
limits make sense?*

1.3.5 Modelling H α

There are 217 quasars in our sample with spectra covering the H α emission line. Below, we use the peak of the H α emission as one estimate of the quasar systemic redshift. In this section we describe how the H α emission was modelled.

The continuum emission is first modeled and subtracted using the procedure described in Chapter ?? . We then test five different models with increasing degrees of freedom to model the H α emission. The models are summarised in Table 1.2. They are (1) a single broad Gaussian; (2) two broad Gaussians with identical velocity centroids; (3) two broad Gaussians with different velocity centroids; (4) two broad Gaussians with identical velocity centroids, and additional narrower Gaussians to model narrow H α emission, and the narrow components of [N II] $\lambda\lambda$ 6548,6584 and [S II] $\lambda\lambda$ 6717,6731; (5) two broad Gaussians with different velocity centroids, and additional narrower Gaussians. If used, the width and velocity of all narrow components are set to be equal in the fit, and the relative flux ratio of the two [N II] components is fixed at the expected value of 2.96. The model we select is the simplest model for which the fractional change in the reduced χ^2 from the model with the lowest reduced χ^2 is less than ten per cent. The numbers of quasars on which each of the five models was applied are given in Table 1.2.

1.3.6 Derived parameters

All [O III] line properties are derived from the [O III] λ 5008 emission, but, as described above, the kinematics of [O III] λ 4960 are constrained by our fitting routine to be identical.

We do not attach any physical meaning to the individual Gaussian components used in the model. Decomposing the [O III] emission in to a narrow component component at the systemic redshift and a

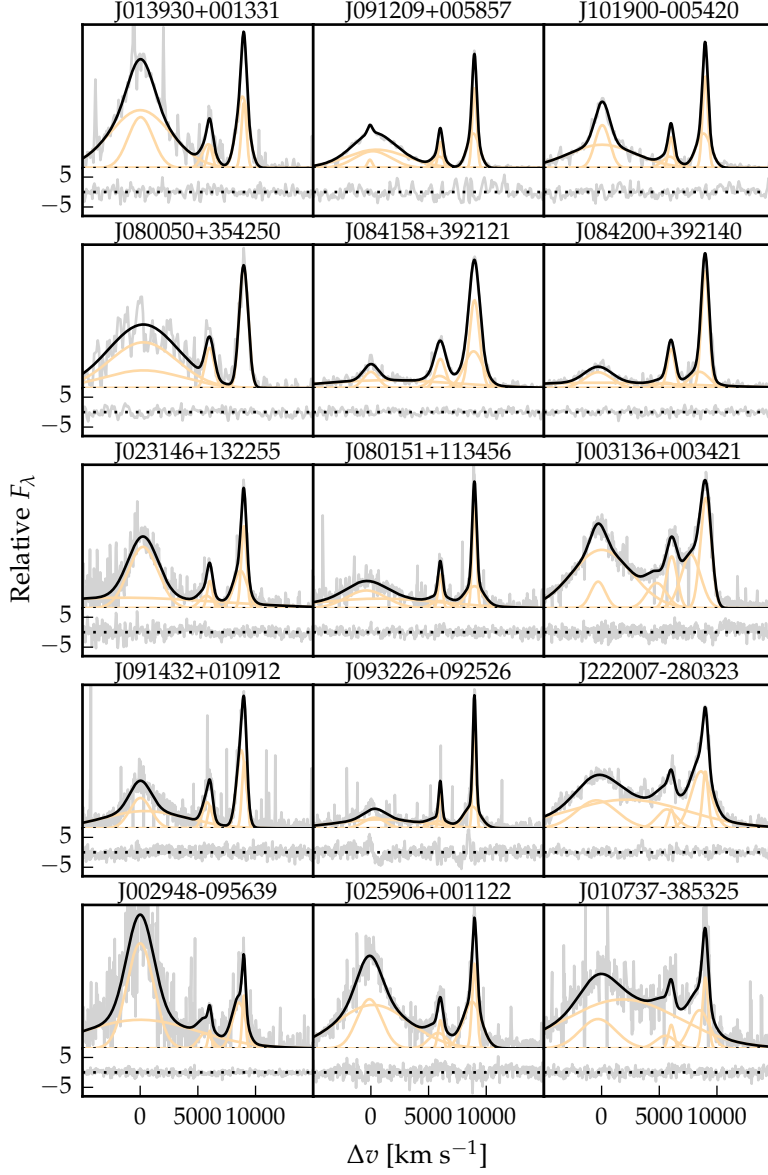


Figure 1.2: Model fits to the continuum- and Fe II-subtracted $H\beta/[O III]$ emission in 15 quasars, chosen at random. The data is shown in grey, the best-fitting model in black, and the individual model components in orange. The peak of the $[O III]$ emission is used to set the redshift, and Δv is the velocity shift from the rest-frame transition wavelength of $H\beta$. Below each spectrum we plot the data minus model residuals, scaled by the errors on the fluxes.

Table 1.3: The format of the table containing the emission line properties from our parametric model fits.

Column	Name	Units	Description
1	UID		Catalogue name
2	OIII_V5	km s^{-1}	[O III] v_5
3	OIII_V5_ERR	km s^{-1}	Uncertainty in v_5
4	OIII_V10	km s^{-1}	[O III] v_{10}
5	OIII_V10_ERR	km s^{-1}	Uncertainty in v_{10}
6	OIII_V25	km s^{-1}	[O III] v_{25}
7	OIII_V25_ERR	km s^{-1}	Uncertainty in v_{25}
8	OIII_V50	km s^{-1}	[O III] v_{50}
9	OIII_V50_ERR	km s^{-1}	Uncertainty in v_{50}
10	OIII_V75	km s^{-1}	[O III] v_{75}
11	OIII_V75_ERR	km s^{-1}	Uncertainty in v_{75}
12	OIII_V90	km s^{-1}	[O III] v_{90}
13	OIII_V90_ERR	km s^{-1}	Uncertainty in v_{90}
14	OIII_V95	km s^{-1}	[O III] v_{95}
15	OIII_V95_ERR	km s^{-1}	Uncertainty in v_{95}
16	z_OIII		[O III] redshift
17	z_OIII_ERR		Uncertainty in [O III] redshift
18	OIII_W50	km s^{-1}	[O III] w_{50}
19	OIII_W50_ERR	km s^{-1}	Uncertainty in [O III] w_{50}
20	OIII_W80	km s^{-1}	[O III] w_{80}
21	OIII_W80_ERR	km s^{-1}	Uncertainty in [O III] w_{50}
22	OIII_W90	km s^{-1}	[O III] w_{90}
23	OIII_W90_ERR	km s^{-1}	Uncertainty in [O III] w_{50}
24	OIII_A		[O III] asymmetry
25	OIII_A_ERR		Uncertainty in [O III] asymmetry
26	OIII_EQW	\AA	[O III] EQW
27	OIII_EQW_ERR	\AA	Uncertainty in [O III] EQW
28	OIII_LUM	erg s^{-1}	[O III] luminosity
29	OIII_LUM_ERR	erg s^{-1}	Uncertainty in [O III] luminosity
30	EQW_FE_4434_4684	\AA	Fe II EQW
31	EQW_FE_4434_4684_ERR	\AA	Uncertainty in Fe II EQW
32	HB_VPEAK	km s^{-1}	H β peak velocity
33	HB_VPEAK_ERR	km s^{-1}	Uncertainty in H β peak velocity
34	HA_VPEAK	km s^{-1}	H α peak velocity
35	HA_VPEAK_ERR	km s^{-1}	Uncertainty in H α peak velocity
36	HB_Z		H β redshift
37	HB_Z_ERR		Uncertainty in H β redshift
38	HA_Z		H α redshift
39	HA_Z_ERR		Uncertainty in H α redshift
40	OIII_REDCHI		Reduced- χ^2 in H β /[O III] fit
41	OIII_FE_FLAG		Bad Fe II subtraction
42	OIII_EXTREM_FLAG		Extreme [O III] emission
43	HA_REDCHI		Reduced- χ^2 in H α fit

lower-amplitude, blueshifted broad component is subject to large uncertainties and is highly dependent on the spectral S/N and resolution. Furthermore, there is no theoretical justification that the broad component should have a Gaussian profile.

We therefore choose to characterize the [O III] line profile using a number of non-parametric measures, which are commonly used in the literature (e.g. Zakamska and Greene, 2014; Zakamska et al., 2016). A normalised cumulative velocity distribution is constructed from the best-fitting model, from which the velocities below which 5, 10, 25, 50, 75, 90, and 95 per cent of the total flux accumulates can be calculated. These velocities are then adjusted so that the peak of the [O III] emission is at 0 km s⁻¹.

The width of the emission line can then be defined using either w_{50} ($\equiv v_{75} - v_{25}$), w_{80} ($\equiv v_{90} - v_{10}$) or w_{90} ($\equiv v_{95} - v_5$). In terms of the FWHM, $w_{50} \simeq \text{FWHM}/1.746$, $w_{80} \simeq \text{FWHM}/0.919$, $w_{90} \simeq \text{FWHM}/0.716$. w_{90} is relatively more sensitive to the wings of the line profile, whereas w_{50} is relatively more sensitive to the core. We also define the relative asymmetry of the line as:

$$A = \frac{(v_{90} - v_{\text{peak}}) - (v_{\text{peak}} - v_{10})}{(v_{90} - v_{10})}. \quad (1.1)$$

Line-width measures are corrected for instrumental broadening by subtracting the resolution of the spectrograph (Table ??) in quadrature. Because the line profiles are typically non-Gaussian, this deconvolution procedure is only approximate. All of the derived parameters we have calculated are summarised in Table 1.3. The columns are as follows:

- 1 Unique ID: QSOXXX.
- 2-3 Systemic redshift measured at [O III] peak wavelength, and its error.
- 4-17 v_5 , v_{10} , v_{25} , v_{50} , v_{75} , v_{90} and v_{95} velocity of [O III], relative to [O III] peak, and their errors, in km s⁻¹.
- 18-23 w_{50} ($\equiv v_{75} - v_{25}$), w_{80} ($\equiv v_{90} - v_{10}$) and w_{90} ($\equiv v_{95} - v_5$) velocity width of [O III], and their errors, in km s⁻¹.
- 24-25 Dimensionless [O III] asymmetry A , and its error.
- 26-27 Rest-frame [O III] EQW, and its error, in Å.
- 28-29 1- σ upper-limit on rest-frame [O III] EQW, in Å.
- 30-31 [O III] luminosity, and its error, in erg s⁻¹.
- 32-33 4434-4684 Å rest-frame Fe II EQW, and its error, in Å.

- 34-35 Velocity of H β peak, relative to [O III] peak, in km s^{-1} , and its error.
- 36-37 Velocity of H α peak, relative to [O III] peak, in km s^{-1} , and its error.
- 38-38 Redshift of H β peak, and its error.
- 40-41 Redshift of H α peak, and its error.
- 42 Reduced χ -squared from [O III]/H β fit.
- 43 Reduced χ -squared in fit to H α .
- 44 Fe II flag.
- 45 Extreme [O III] flag.
- 46-47 C IV v_{50} , relative to [O III] peak, in km s^{-1} , and its error.

1.3.7 *Deriving uncertainties on parameters*

Our method to estimate realistic uncertainties on emission line properties derived from the best-fitting model is very similar to the one describe in Chapter ?? . Very briefly, random simulations of each spectrum are generated. Our fitting-procedure is run on each simulated spectrum, and the errors on the line parameters are estimated by looking at the distribution of values from the ensemble of simulations. In a slight modification of the procedure in Chapter ?? , the error is defined using the 68 (84 - 16) percentile spread in the parameter values.

1.3.8 *Low EQW [O III]*

In Figure 1.3 we show how the uncertainty in v_{10} depends on the EQW. As the strength of [O III] decreases, the average uncertainty in v_{10} increases. As the EQW drops below 8\AA , typical uncertainties in v_{10} become very large (exceeding 1000km s^{-1} in many objects). Clearly, the emission line is too weak for properties - in this case v_{10} - to be reliably measured in many of these objects. Therefore, when the [O III] line shape is analysed in later sections, these objects with $\text{EQW} < 8\text{\AA}$ will be excluded.

1.3.9 *Reliability of redshift estimates*

In this section we do a comparison of systemic redshift estimates from [O III], broad H β and H α . The wavelength of each of these lines is measured at the peak of the emission. This measurement is done on the best-fitting parameter model. In the case of the Balmer lines, this model includes both broad and narrow emission features.

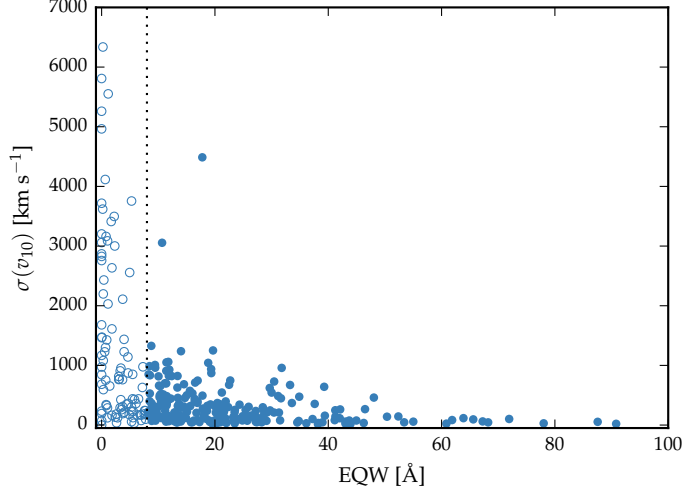


Figure 1.3: Uncertainty in v_{10} as a function of the EQW, for [O III]. Uncertainties in v_{10} are large to the left of the vertical line, at 8\AA . These objects are ignored in our subsequent analysis of the [O III] line shape.

The redshift comparison is shown in Figure 1.4. We compare systemic redshift estimates based on [O III] and H β (Figure 1.4a), [O III] and H α (Figure 1.4b) and H β and H α (Figure 1.4c). In (a) and (b) we consider only the subset of objects with [O III] detections that do not suffer from poor Fe II subtraction or have extreme [O III] profiles (210 quasars). The available spectroscopic data extends to H β and H α for 204 and 99 of these objects respectively. Spectroscopic data that covers both H β and H α is available for 219 quasars. We also exclude objects with extremely large peak wavelength uncertainties due to poor spectra S/N. We choose cut-offs of 750, 400 and 400 for errors on the H β , H α and [O III] peaks respectively. This leaves 187, 85 and 142 objects in samples (a), (b) and (c) respectively.

We generate probability density functions using a Gaussian kernel density estimator. The bandwidth, which is optimised using leave-one-out cross-validation, is 170, 140 and 140 km s^{-1} for (a), (b) and (c) respectively. The means (medians) of the distributions shown in (a), (b) and (c) are -120 (-90), -90 (-40) and 20 (40) km s^{-1} . The standard deviations are 360, 300 and 250 km s^{-1} . The scatter in these distributions is consistent with previous studies of redshift uncertainties from broad emission lines (e.g. Shen et al., 2016).

Paul: what can I say about these results?

1.4 RESULTS

In our sample of 354 quasars, there is a huge diversity in [O III] emission properties (Fig. 1.2). Properties of the [O III] emission (EQW, w_{80} and asymmetry) are shown in Figure 1.5.

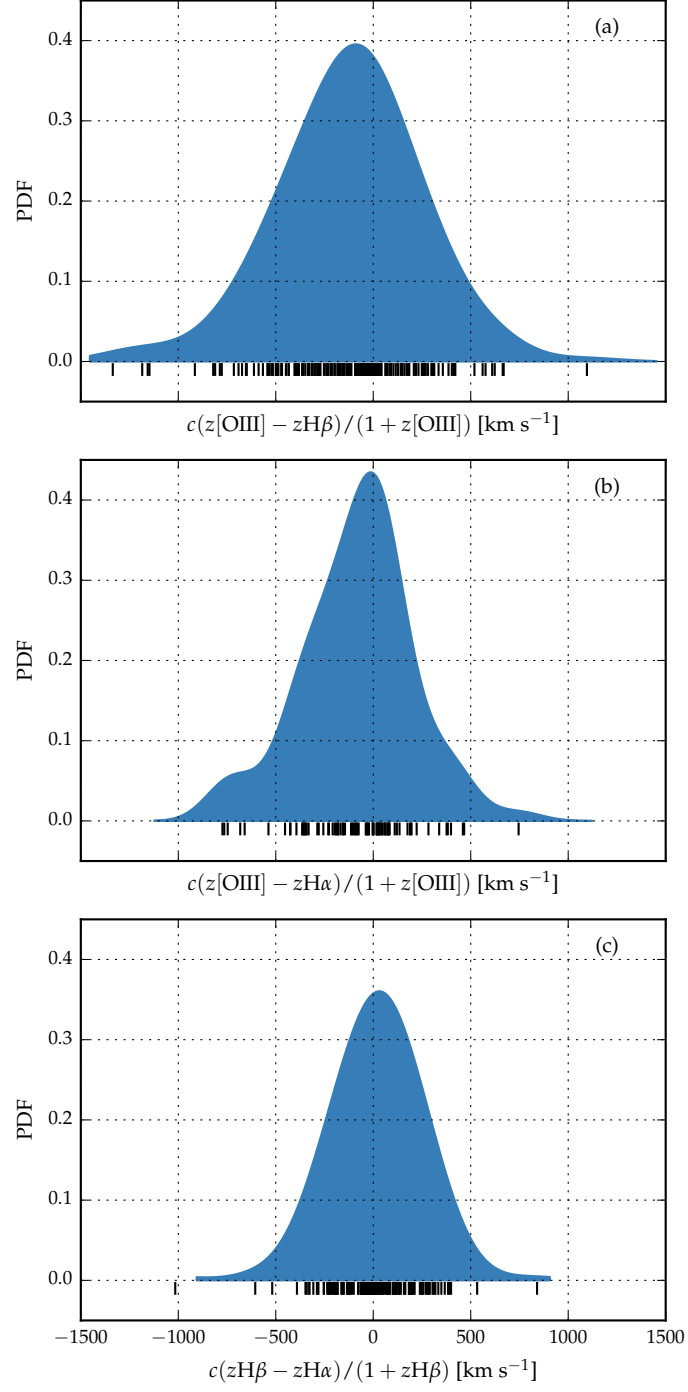


Figure 1.4: Comparison of systemic redshift estimates using [O III], broad H β and broad H α . The probability density functions are generated using a Gaussian kernel density estimator with a $\simeq 150 \text{ km s}^{-1}$ kernel width. The short black lines show the locations of the individual points.

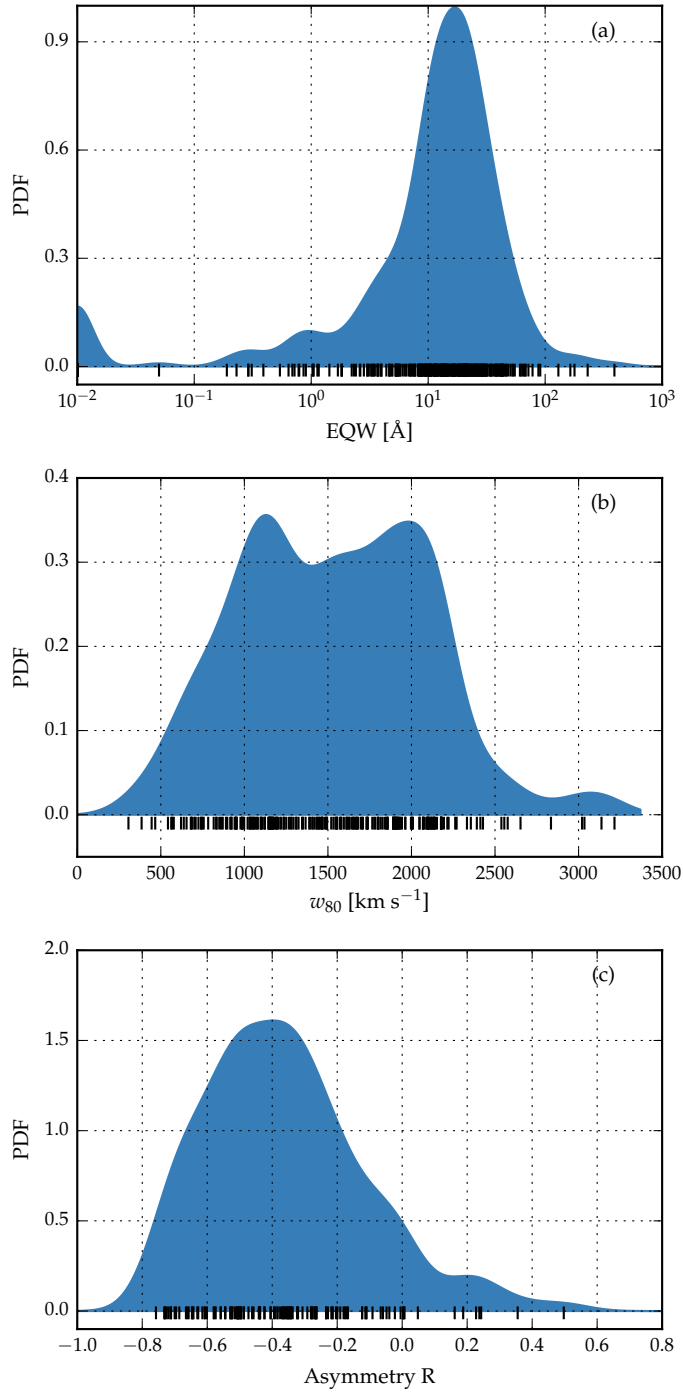


Figure 1.5: Correlations between the line width w_{80} , asymmetry R and EQW of [O III].

Paul: How to define
undetected?

The [O III] EQW follows an approximately log-normal distribution, peaking at 17\AA . In XX per cent of our sample [O III] is very weak, with $\text{EQW} < \text{XX}\text{\AA}$.

The width of [O III], here characterised by w_{80} , has a very broad distribution, with extremes at 300 and 3000 km s^{-1} . The 1200 km s^{-1} upper limit on the velocity width of the Gaussian functions used to model [O III] is responsible for the peak at 1200 km s^{-1} .

The [O III] asymmetry is shown in Figure 1.5c. In 40 per cent of the sample [O III] is fit with a single Gaussian. The asymmetry is zero in this model and so these objects are excluded. [O III] is blue-asymmetric in all but a handful of objects.

1.4.1 Luminosity/redshift-evolution of [O III] properties

In this section we compare the [O III] properties of our quasar sample with a sample of AGN at lower redshifts with lower luminosities. [O III] is broader, which is consistent with these quasars having more massive BHs. [O III] also shows stronger blue asymmetries, suggesting that outflows are stronger/more prevalent at these higher luminosities/redshifts. The luminous blueshifted broad wing and the extremely broad profile reveals high-velocity outflowing ionized gas. Our results therefore suggest that kilo-parsec-scale outflows in ionized gas are common in this sample of high-luminosity, high-redshift quasars.

1.4.1.1 Equivalent width

In Fig. 1.6 we show the [O III] EQW as a function of the quasar bolometric luminosity. Bolometric luminosity is estimated from the monochromatic continuum luminosity at 5100\AA , using the correction factor given by Richards et al., (2006). For comparison, we also show the low- z sample from Shen et al., (2011).

We find that [O III] EQW is fairly constant as a function of quasar luminosity in the objects with prominent [O III] emission. However, the proportion of objects in which [O III] is undetected is much larger in the higher luminosity sample (e.g. Netzer et al., 2004). Netzer et al., (2004) found 1/3 of their high luminosity sample had very weak [O III], whereas quasars with weak [O III] are very rare for nearby AGN. We find that [O III] is undetected/very weak in XX per cent of our sample, which is very similar to the fraction reported by Netzer et al., (2004). As a result, the mean [O III] EQW decreases as a function of luminosity (e.g. Brotherton, 1996; Netzer et al., 2004; Sulentic et al., 2004; Baskin and Laor, 2005).

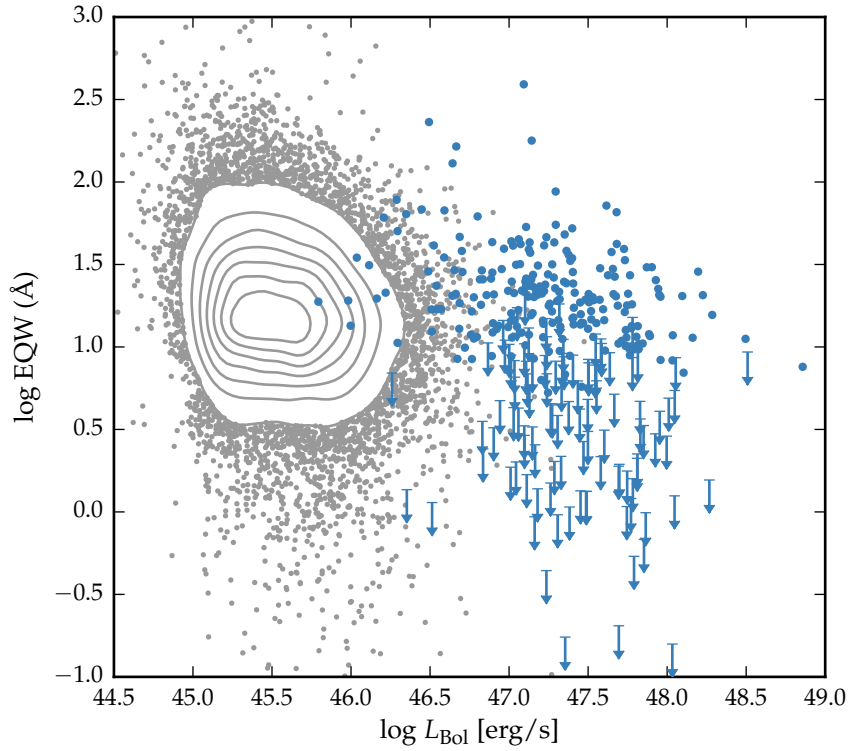


Figure 1.6: The [O III] EQW as a function of the quasar bolometric luminosity for the sample presented in this chapter (blue circles) and the low- z SDSS sample (grey points and contours). Upper limits are denoted by the downward arrows. **Paul: When should upper limits be used? At the moment I'm using $< 8 \text{ \AA}$, but this was defined as the cut-off to measure w_{80} .**

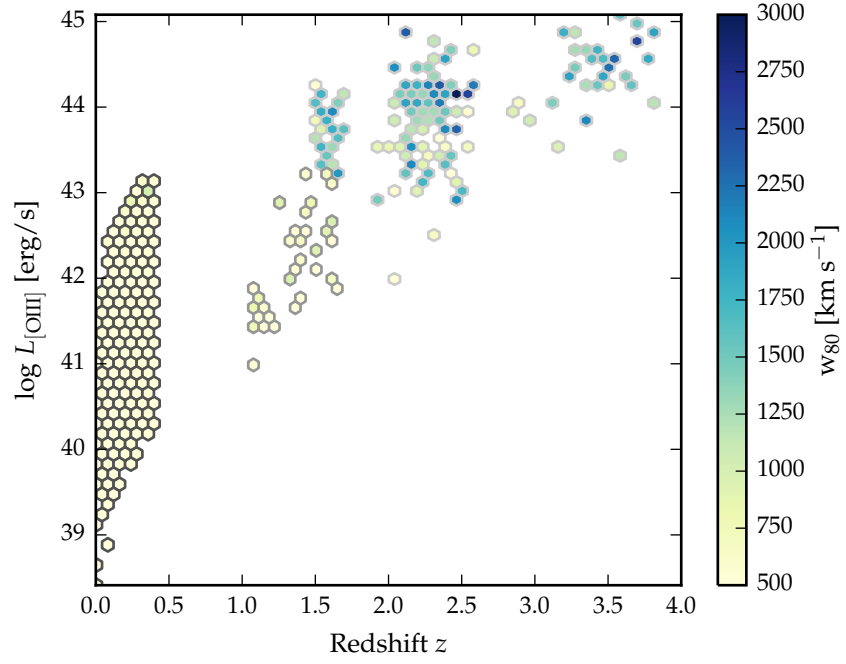


Figure 1.7: The [O III] velocity-width, characterised by w_{80} , as a function of the [O III] luminosity and the quasar redshift. The colour of each hexagon denotes the mean w_{80} for the objects in that luminosity-redshift bin. We have supplemented our sample with low- z objects from Zakamska and Greene, (2014) and medium ($z \sim 1.5$) redshift objects from Harrison et al., (2016).

1.4.2 Velocity width

In this section we look for any luminosity/redshift dependent changes in the [O III] line properties. To do this we extend the dynamic range of our samples in terms of both luminosity and redshift by supplementing our sample with quasars presented by Mullaney et al., (2013) and Harrison et al., (2016). They are selected to have [O III] luminosities above $10^{8.5} L_{\odot}$ and have a median redshift $z = 0.397$. The Mullaney et al., (2013) catalogue contains [O III] line measurements for $\sim 25\,000$ SDSS spectra. We select only the Type I AGN. The Harrison et al., (2016) sample contains 40 quasars at intermediate redshifts ($1.1 \leq z \leq 1.7$).

In Figure 1.7 we show the [O III] velocity width as a function of the [O III] luminosity and the quasar redshift. The lack of any redshift-evolution between $z = 0$ and $z = 1.5$ was reported by Harrison et al., (2016). On the other hand, at fixed redshift, we see a significant correlation between the [O III] velocity width and the luminosity.

1.4.3 Eigenvector 1 correlations

The FWHM of the broad H β emission line and the relative strengths of optical Fe II and H β have been identified as the features responsible for the largest variance in the spectra of AGN. These parameters form part of EV₁, the first eigenvector in a PCA which originated from the work of Boroson and Green, (1992). The underlying driver behind EV₁ is thought to be the Eddington ratio (e.g. Sulentic et al., 2000; Shen and Ho, 2014).

In Figure 1.8 we show the [O III] EQW as a function of the H β FWHM and the optical Fe II strength. The optical Fe II strength is defined as the ratio of the Fe II and H β EQW, where the Fe II EQW is measured between 4434 and 4684 Å. Measurements of the H β line properties are taken from Chapter ?? . In our sample, these parameters follow very similar correlations to what is observed at low- z (see also Sulentic et al., 2004; Shen, 2016). In particular, we observe a strong anti-correlation between the [O III] and Fe II EQW. The H β FWHM are displaced to higher values, which is consistent with the high-redshift, high-luminosity sample having larger BH masses.

These emission line trends in the optical (for low- z quasars) can be extended to UV emission lines observed at higher redshifts. The C IV blueshift and EQW is a diagnostic that similarly spans the diversity of broad emission line properties in high redshift quasars (dominated by a virialized component at one extreme and a wind driven component at the other Richards et al., 2011; Sulentic et al., 2007). The similarity of the C IV EQW-blueshift parameter space at high redshift to EV₁ parameter space at low redshift suggests that these trends are connected.

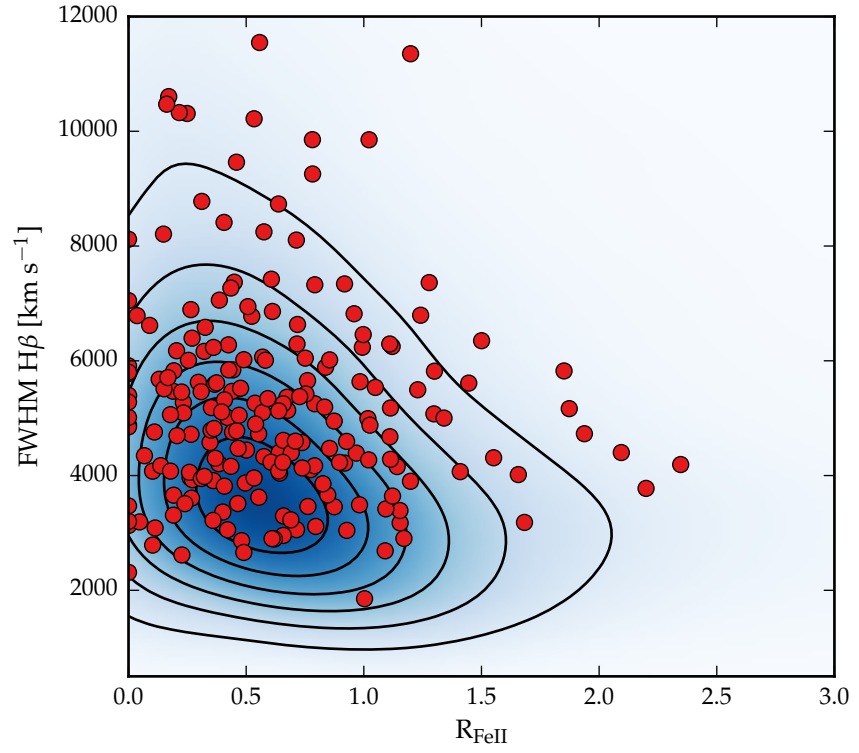


Figure 1.8: EV1 parameter space. The contours and shading show low-redshift, low-luminosity SDSS AGN (with measurements taken from Shen et al., (2011)) and the red circles show the high-redshift, high-luminosity objects presented in this chapter.

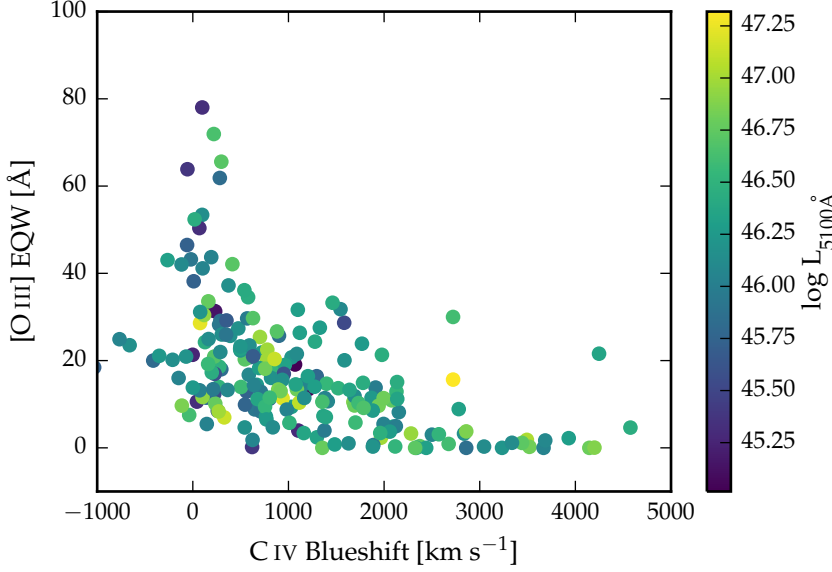


Figure 1.9: [O III] EQW as a function of the C IV blueshift.

Can we calculate a mapping between the two parameter spaces? As a first step we show how the EV1 parameters change as a function of position in the C IV EQW-blueshift parameter space in Figure 1.10. Optical spectra are available for XXX quasars in our catalogue, and cover the broad C IV doublet. As we described in Chapter ??, C IV is often blueshifted, which almost certainly signals the presence of strong outflows, most likely originating in a disc wind. In Chapter ?? we demonstrated that the quasars in our sample cover the full range of C IV blueshifts seen in the SDSS quasar population, which makes our sample unique in that it allows us to study properties of the quasar across the full parameter range. The C IV blueshift is measured relative to the redshift determined from the peak of [O III], H β or H α . Two hundred and fourteen objects are shown in Figure 1.10. Objects flagged as having significant Fe II residual emission have been removed. Objects for which the H β or C IV line properties could not be measured reliably (see Section ??) have also been removed. Finally, we consider only objects for which the C IV EQW exceeds 15 Å.

Most of the diversity in C IV properties is correlated with the [O III] EQW. This is seen more clearly in Fig. 1.9, in which we plot the [O III] EQW as a function of the C IV blueshift.

On the other hand, the C IV blueshift and EQW cannot be used to predict the H β FWHM. This is consistent with what we found in Chapter ??: objects with large C IV blueshifts have narrow Balmer emission lines, but objects with modest C IV blueshifts have a wide range of Balmer line widths.

We see a correlation between the [O III] velocity width and asymmetry. As the line gets broader it gets more blue-asymmetric. One

interpretation of this is that the strength of the narrow core is decreasing, leading to a broader and more blueshifted profile (e.g. Shen and Ho, 2014).

1.4.3.1 Extreme [O III] emitters

Extreme [O III] velocity widths have been extremely red quasars (e.g. Zakamska et al. 2016; Hamman et al. 2016b) and obscured quasars (Brusa et al. 2015).

Figure 1.11 shows the spectra of 18 objects which we visually identified as having exceptionally broad [O III] emission profiles. These objects are defined as having very broad [O III] emission (although not necessarily the broadest in our sample) and heavily blended emission in between the zero-velocity wavelengths of H β and [O III]. In Figure 1.12 we show that these objects all have high luminosities.

Paul/Manda: Is this interesting? Just following trend of non-extreme objects?

These [O III] emission lines are similar to the lines observed in a sample of four extremely dust-reddened quasars at $z \sim 2$ recently identified by Zakamska et al., (2016). The extreme nature of the [O III] emission in these objects led Zakamska et al., (2016) to propose that these objects are being observed transitioning from a dust-obscured, star-burst phase to a luminous, blue quasar. A similar [O III] emission was also observed in J1201+1206 in a sample of five of the most luminous quasars at redshifts $2.3 \lesssim z \lesssim 3.5$ observed by Bischetti et al., (2016).

We matched our catalogue to the AllWISE release from WISE with a 5'' matching radius. Out of 259 quasars, matches were found for 249. We did a linear interpolation through the WISE SED to find the flux at rest-frame 5 μ m, which we then convert in to a monochromatic luminosity. The four Zakamska et al., (2016) quasars have 5 μ m luminosities of $\sim 10^{47}$ erg/s, which is comparable to maximum luminosity of our sample. The [O III] velocity widths of the Zakamska et al., (2016) objects are extreme in relation to our sample, matched in 5 micron luminosity. The typical dust reddening in our sample is small (~ 0.03 by fitting Maddox et al. SED model).

It is impossible to determine unambiguously what combination of H β , [O III] and Fe II is responsible for the unusual plateau-like emission observed in these objects.

1.4.4 [O III] and C IV outflows are linked

We have already seen how [O III] is broader and more blueshifted in more luminous quasars. However, at a given luminosity, what else controls the [O III] line properties? It has been known for some time that the [O III] EQW is anti-correlated with the strength of optical Fe II, and this trend is thought to be driven by the Eddington ratio. Shen and Ho, (2014) showed that the amplitude of the core [O III] emission decreases faster than the wing component as the Eddington

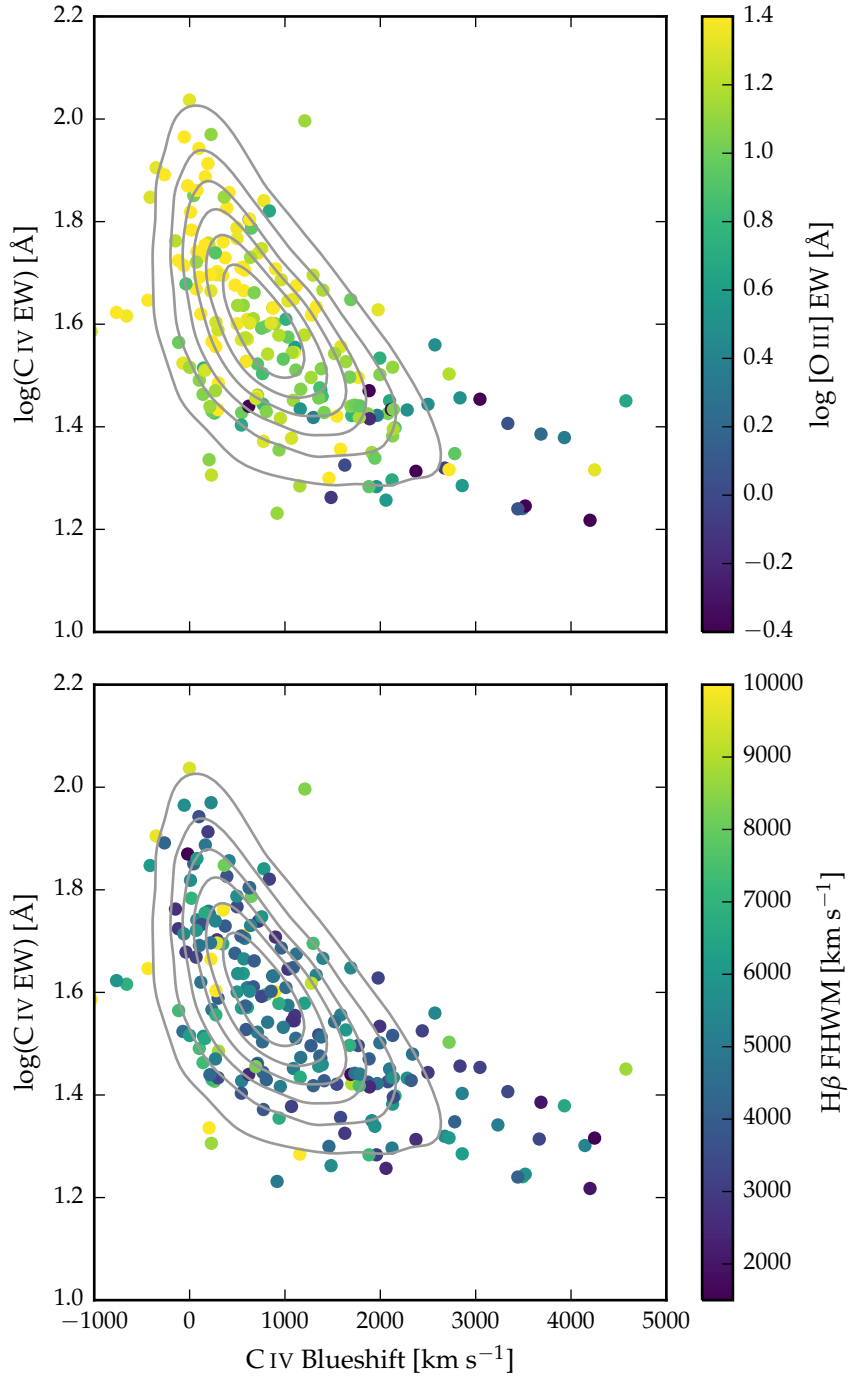


Figure 1.10: The high-redshift EV1 parameter space of C IV blueshift and EQW. Our sample is shown with points, and quasars from the full SDSS catalogue are shown with grey contours. The [O III] EQW varies systematically with position in the C IV blueshift-EQW parameter space (a) but the Hβ FWHM shows significantly less systematic variation (b).

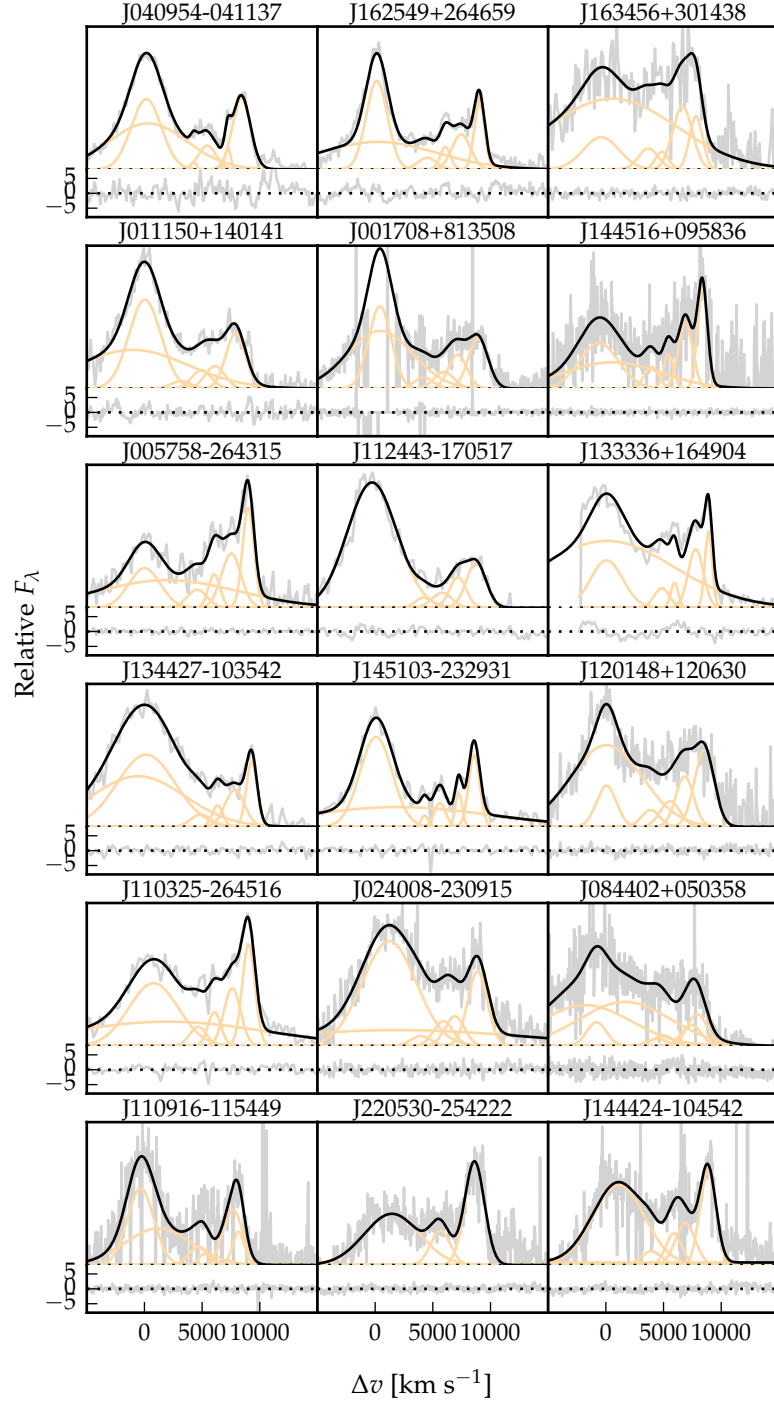


Figure 1.11: Model fits to the continuum- and Fe II-subtracted $H\beta/[O\text{ III}]$ emission in 18 quasars with extreme $[O\text{ III}]$ emission profiles. The data is shown in grey, the best-fitting model in black, and the individual model components in orange. The peak of the $[O\text{ III}]$ emission is used to set the redshift, and Δv is the velocity shift from the rest-frame transition wavelength of $H\beta$. Below each spectrum we plot the data minus model residuals, scaled by the errors on the fluxes.

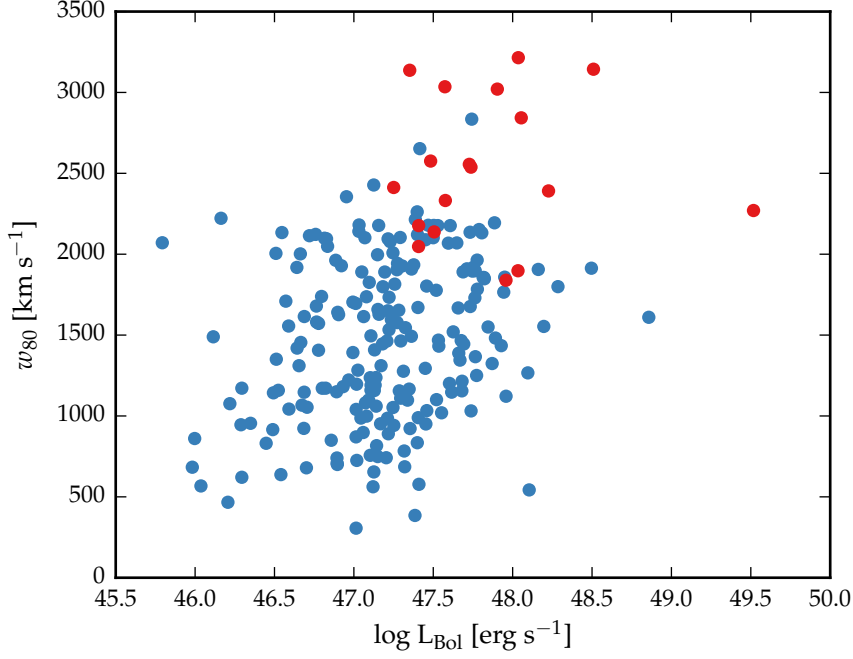


Figure 1.12: [O III] velocity width as a function of quasar bolometric luminosity. Objects with extreme [O III] profiles are shown in red.

ratio increases. Therefore, the [O III] emission is weaker and more blueshifted in high accretion rate quasars. In Chapter ?? we found that all quasars with strong BLR outflows have high Eddington ratios. In this section, we show that the C IV and [O III] blueshifts are directly linked. This suggests a direct connection between the gas kinematics in the broad and narrow line regions.

As described above, C IV emission properties are available for XX quasars in our sample. We use the C IV velocity centroid measurements we derived in Chapter ?. We take a subset of quasars with [O III] EQW $> 8\text{\AA}$. We also remove objects where the fractional uncertainty on v_{10} exceeds 50 per cent (XX quasars).

In Figure 1.13 we show the C IV blueshifts against the [O III] blueshifts. There is a clear and strong correlation. The EQW cut removes most of the quasars with large C IV blueshifts, since [O III] is on average very weak in these quasars. Similar correlations have been tentatively found in lower redshift quasars and AGN (Zamanov et al., 2002).

The blueshifting of C IV is known to correlate with luminosity (Richards et al., 2011). In [O III], the blueshifted wing becomes relatively more prominent as the luminosity of the quasar increases (Shen and Ho, 2014). Therefore, it is plausible that the correlation between the C IV and [O III] blueshifts is a secondary effect that is driven by the correlation of each with the luminosity. However, no strong luminosity-dependent trends are apparent in Figure 1.13. We

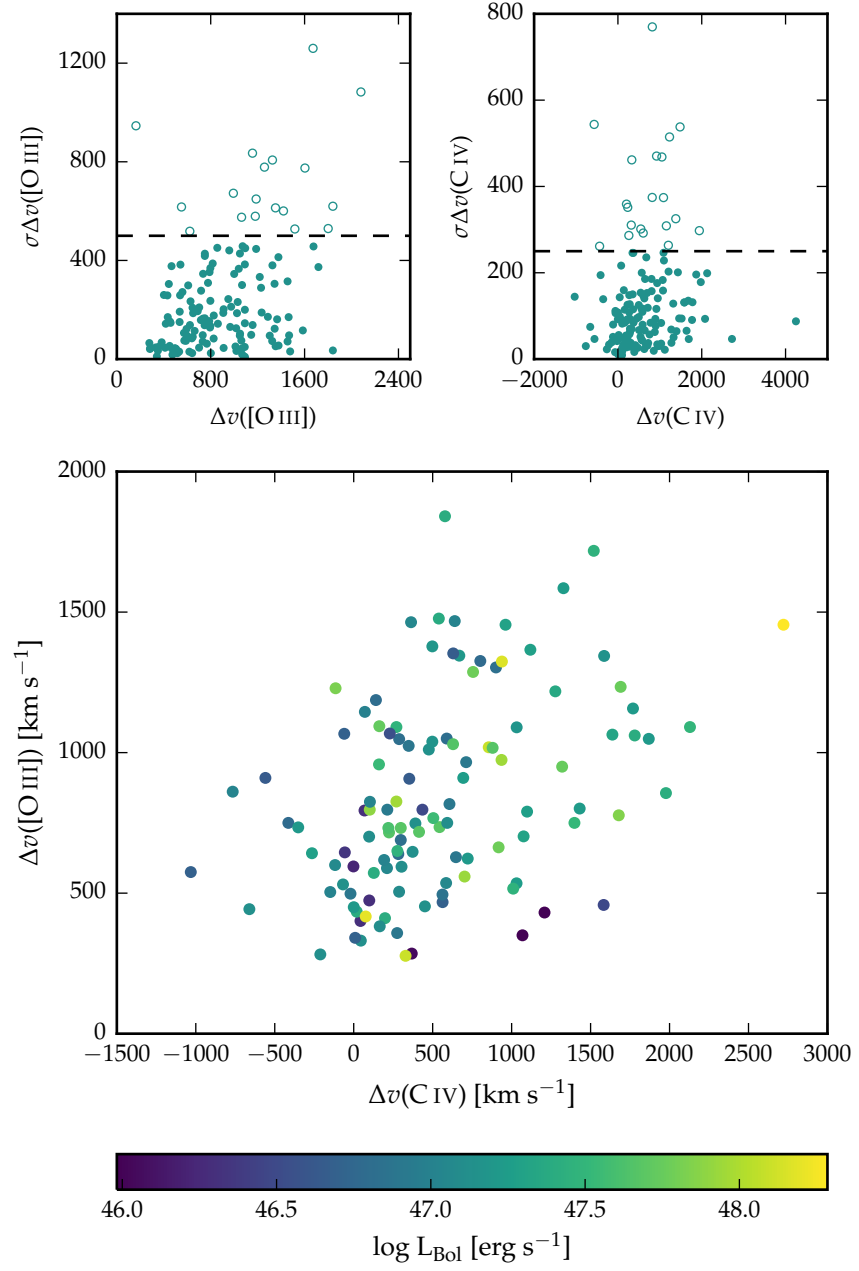


Figure 1.13: The relation between the blueshifts of C IV and [O III].

find that both the [O III] and C IV blueshifts are correlated with the luminosity, but that these correlations are much weaker than the correlation between the [O III] and C IV blueshifts.

The [O III] ‘blueshift’ is parametrized using as $v_{10} - v_{\text{peak}}$. For the C IV blueshift we use v_{50} as a measure of the line location, and again use the peak of the [O III] emission to define the systemic redshift. This is consistent with the definition we use in Chapter ?? . We considered a number of alternative approaches to parametrising both the [O III] line shape and the systemic redshift. As expected, very similar trends are observed when the [O III] line shape is parametrized using $v_{25} - v_{\text{peak}}$, $v_{50} - v_{\text{peak}}$, $w_{80} = v_{90} - v_{10}$, or the relative asymmetry R .

The same trend is also observed when the systemic redshift is defined using the peak of the H β emission.

*Discuss cuts
We don't show
extreme objects*

1.5 DISCUSSION

Looking at the [O III] velocity width as a function of luminosity tells us about the physical drivers of the outflows observed in [O III]. The correlation with luminosity suggests that the highest velocity outflows are associated with the most luminous AGN. This has been reported for low-redshift AGN, for both ionized and molecular outflows (e.g. Westmoquette et al. 2012; Veilleux et al. 2013; Arribas et al. 2014; Ciccone et al. 2014; Hill & Zakamska 2014).

This suggests that the outflows are driven by radiative forces. On the other hand, Mullaney et al., (2013) find that once the correlation between the [O III] luminosity and the radio luminosity has been taken in to account, the [O III] velocity width is more strongly related to the radio luminosity of the AGN.

Is the AGN NLR absent in objects where outflows have reached kilo-parsec scales, sweeping up the low-density material responsible for the [O III]-emission? If the BLR outflows can escape, they are very fast and wouldn't need long to clear out the NLR gas. .

*Manda/Paul:
Estimate a
time-scale for how
long the NLR would
take to be cleared
given typical size of
galaxy and velocity
of outflow*

1.6 ICA

Then having presented the main results, I would go on to discuss the limitations of the Gaussian approach - e.g. FeII can't be properly subtracted in many cases and sensitive to S/N - and use this as an intro to the much more flexible ICA method. You could then have a much briefer description of the ICA reconstructions and present this more as work in progress. You could show that your main results (as above) still hold with the ICA (e.g. Figs 1.15, 1.16, 1.17) and that this allows you to solve the FeII problem and push to lower SNR. Finally, you could discuss some of the potential improvements to the ICA components that would allow the derived line properties from

the ICA to become even more robust. ICA works better at low S/N because we are effectively putting priors on the model parameters.

The second model consists of six spectral components derived from an ICA of a large sample of low-redshift AGN with SDSS spectra covering the same spectral region. As we will demonstrate, a linear combination of these spectral components is able to reproduce the spectra around $H\beta/[O III]$ to a high degree of precision.

1.6.1 Model Two: Independent Component Analysis

ICA is a blind source separation technique for separating a signal in to linearly mixed statistically independent subcomponents. Unlike the more widely-used principle component analysis technique, ICA produces non-negative components which allows for a physical interpretation of the components and weights. ICA has been successfully applied to model the spectra of emission-line galaxies (Allen et al., 2013) and BAL quasars (Allen et al., 2011). The quasar spectra can be thought of as a set of observations, \mathbf{x} , which are made up of statistically independent components, \mathbf{c} , that are combined by some mixing matrix, \mathbf{W} :

$$\mathbf{x} = \mathbf{W}\mathbf{c} \quad (1.2)$$

ICA reverses this process and describes how the observed data are generated. Both the independent components and the mixing matrix are unknown, but can be found by solving:

$$\mathbf{c} = \mathbf{W}^{-1}\mathbf{x}. \quad (1.3)$$

Ask Paul for details.

The components were solved for using a sample of 2,154 SDSS quasars at redshifts XX . At these redshifts the SDSS spectrograph covers the rest-frame region $XX-XX\text{\AA}$ where $H\beta$ and $[O III]$ lie. The individual spectra were first adjusted to give the same overall shape as a model quasar template spectrum. Six positive independent components and four additional components that could be negative were found to be sufficient to reconstruct the spectrum, without over-fitting. Each quasar spectrum \mathbf{x}_j can then be represented as a linear combination of the independent components:

$$\mathbf{x}_j = \sum_{i=1}^{10} c_{ij} \mathbf{W}_{ij} \quad (1.4)$$

1.6.1.1 Fitting procedure

Each of the individual ICA components has been adjusted to give the same overall shape as a quasar template spectrum. We approximate the overall shape of this template by fitting a single power-law

to emission line free windows at 4200-4230, 4435-4700 and 5100-5535 Å. We then flatten each of the ICA components by dividing by this power-law. An identical process is performed on each spectrum we fit, so that both the components and the spectrum to be fitted have essentially zero shape. For each quasar in our sample we perform a variance-weighted least-squares minimisation to determine the optimum value of the components weights. The first six component weights are constrained to be non-negative, and the fit is done in logarithmic wavelength space, so that each pixel corresponds to a fixed velocity width. The relative shift of the ICA components is also allowed to vary in the optimisation procedure, to account for errors in the systemic redshifts used to transform the spectra in to rest-frame wavelengths.

1.6.1.2 Quality of fits

In general, the ICA components do a remarkably good job at reconstructing the spectra of the objects in our sample. For example, in J125141+080718 (discussed above), it does much better job at modelling the Fe II emission than the Boroson and Green, (1992) template. It is less sensitive to the spectral S/N, and the component weights do not need to be constrained. It is therefore much simpler to apply than fitting multiple Gaussians.

*Don't say
remarkable
Is there some way to
demonstrate/quantify
this?*

However, it does have its limitations. The components were calculated using a set of lower-redshift, lower-luminosity AGN, and quasar spectra are known to vary systematically as a function of luminosity. For example, the [O III] line is typically broader in more luminous quasars. Because there are so few objects with very broad [O III] in the low-redshift sample, the ICA reconstruction fails to reproduce the broadest [O III] profiles in our sample.

1.6.2 Physical interpretation of ICA components

Although the ICA analysis is not based on any physics, there appears to be a direct correspondence between the individual components and the different emission features which contribute to the spectra (Fig. 1.14). This correspondence is summarised in Table 1.4. The component w_1 seems to correspond to Fe II emission, the components w_2 and w_3 to broad H β emission, the components w_4 and w_5 to narrow [O III] emission at the systemic redshift, and the component w_6 to broad, blueshifted [O III] emission.

1.6.2.1 Reconstructing the [O III] profile

In order to measure non-parametric line parameters, e.g. v_{10} , we must first reconstruct the [O III] emission. It is fortunate that most of the [O III] emission is in just three of the ICA components; the remain-

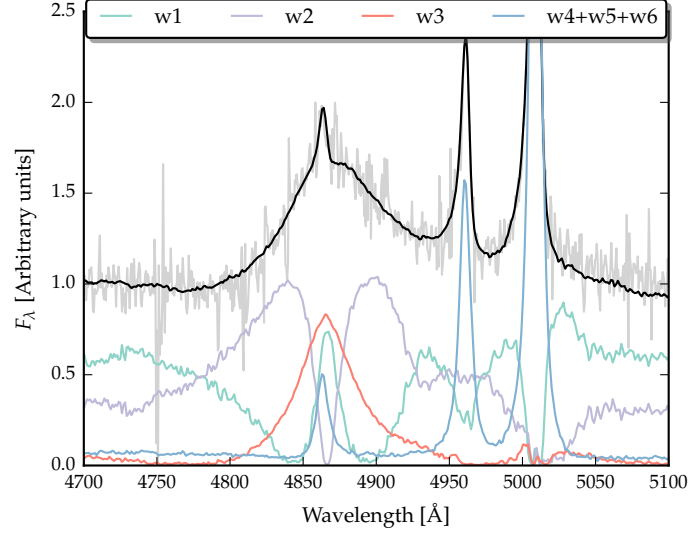


Figure 1.14: $H\beta/[O\text{ III}]$ emission J002952+020607. The ICA reconstruction is shown in black, and the spectrum in grey. The first three components, and the sum of components four, five and six are shown individually.

Table 1.4: Physical interpretation of the ICA components.

Component	Origin
w_1	Fe II
w_2	$H\beta$
w_3	$H\beta$
w_4	[O III] core
w_5	[O III] core
w_6	[O III] wing

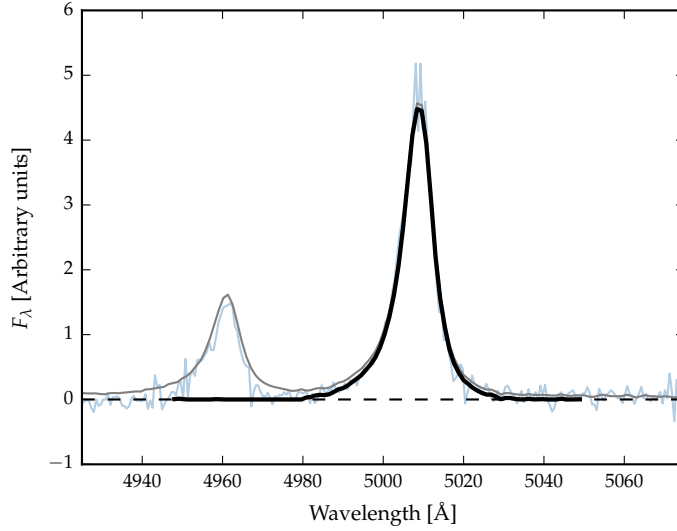


Figure 1.15: [O III] emission in J002952+020607. The data is shown in blue, and the ICA spectrum in grey. The first three ICA components have been subtracted from both the ICA composite and the data. The black curve shows the reconstructed [O III] profile.

ing three contribute very little. Therefore, we can set the first three weights to zero to leave only the [O III] emission. The four correction components are also included.

We define the boundaries of [O III] λ 5008 as being between 4950 and 5500Å. The blue limit is close to the peak of the [O III] λ 4960 line, and so to recover the intrinsic profile we instead use the blue wing of [O III] λ 4960. We use the emission from 4980-5050Å, and from 4900-(4980-(5008.2-4960.3)). The blue window is then shifted by (5008.2-4960.3) to reconstruct the blue wing of the [O III] λ 5008 line. We then subtract a constant, because the flux does not always go to zero (suggests that there is probably flux which is not due to [O III] emission in components four to six).

An examples of a reconstructed [O III] emission line is shown in Figure 1.15. *At present I am summing the flux all the way from 4950Å. However, this is quite a lot of flux to sum up, and we can't ascribe this flux to the wing of the [O III] emission with any certainty. This is borne out by the fact that there are quite large differences between, for example, v_{10} measured from the Gaussian fit and v_{10} measured from the ICA fit.*

Unfortunately, there are systematic differences between the line-width estimates from the Gaussian reconstructions and the ICA reconstructions, particularly for broad-line objects. The current way of doing the ICA reconstruction of the [O III] line ignores any cross-talk between the components and there is potentially flux being ascribed to the line that could be coming from some other component. We can solve this by finding some more representative broad [O III] lines in

SDSS from which to derive the components as well as producing a set of components for [O III] only. Therefore we don't use these reconstructions and leave this for future work.

1.6.3 ICA fits

In Figure 1.16 we show the relative weights of each of the six positive ICA components. Also shown are the same measurements for a sample of low-redshift, low-luminosity AGN. We want to examine whether or not there are systematic differences between these two samples.

We see that [O III] core emission is weaker in the more luminous sample, but the strength of the wing component is similar. Shen and Ho, (2014) showed that the strength of the core [O III] component decreases with quasar luminosity and optical Fe II strength faster than the wing component, leading to overall broader and more blueshifted profiles as luminosity and Fe II strength (or C IV blueshift) increases. Shen and Ho, (2014) suggested that a stable NLR is being removed by the outflowing material. Similarly, Zhang et al., (2011) found that the more the peak of the [O III] line is blueshifted, the more the core component decreases dramatically, while the blue wing changes much less. Therefore, there is an anti-correlation between the strength of the core component and the relative strength of the wing component (Figure 1.18).

To show this phenomenon more clearly, we plot the relative [O III] strength and the [O III] wing/core ratio in the high/low luminosity samples (Figure 1.18). We see that [O III] is weaker in the high luminosity sample, but that the wing component is much stronger relative to the core component. .

Similar to behaviour of C IV? Would suggest that the mechanism producing the two correlations is the same

1.6.3.1 EV1 correlations

In Figure 1.19 we show how the [O III] strength varies as a function of the C IV blueshift. There is a very well defined relation: when C IV is strongly blueshifted [O III] is very weak. This is very similar to what we found when we used Gaussian functions to model the emission. The correlation between C IV blueshift and [O III] EQW is shown in a different way in Figure 1.20. Here we divide our sample in to four bins according to the C IV blueshift. From the quasars in each C IV blueshift bin we then find then generate an ICA spectrum using the median weights from each quasar. The differences in the spectra as a function of the C IV blueshift are dramatic. [O III] becomes progressively weaker and more blueshifted. The anti-correlation with Fe III and the blue-ward Fe II also clear, but there is no change in the red-ward Fe II.

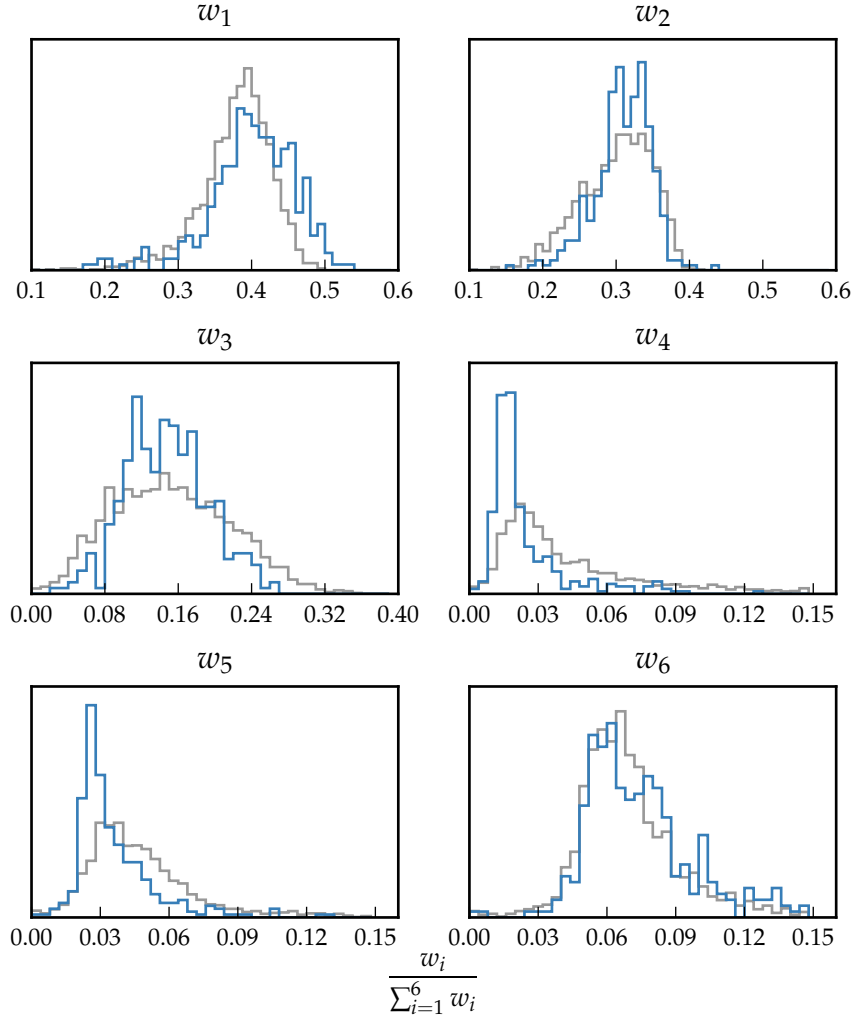


Figure 1.16: The relative weight in each of the six positive ICA components for the high-luminosity (blue) and low luminosity samples (grey). In the high-luminosity sample Fe II emission is stronger (component w_1). The core [O III] emission (components w_4, w_5) is weaker but the strength of the blueshifted wing (w_6) is the same.

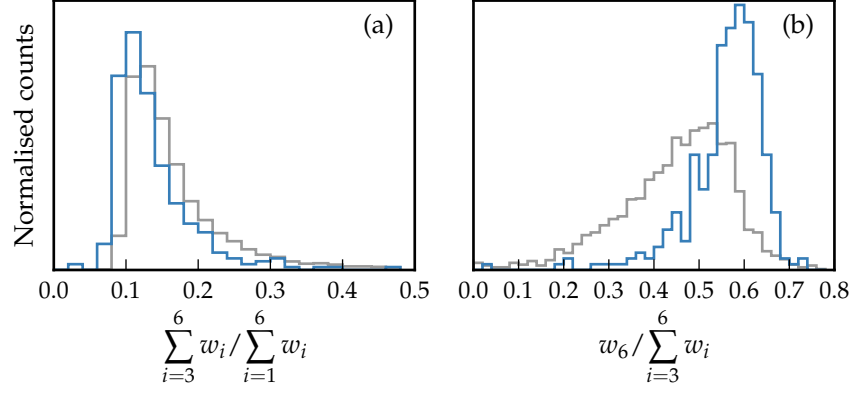


Figure 1.17: The relative weight in the three ICA components corresponding to [O III] emission (*left*) and the relative weight of the component most closely related to blueshifted [O III] emission relative to all three [O III] components (*right*). [O III] emission is weaker in the high-luminosity sample, but the relative contribution from the blueshifted component to the total [O III] emission is higher.

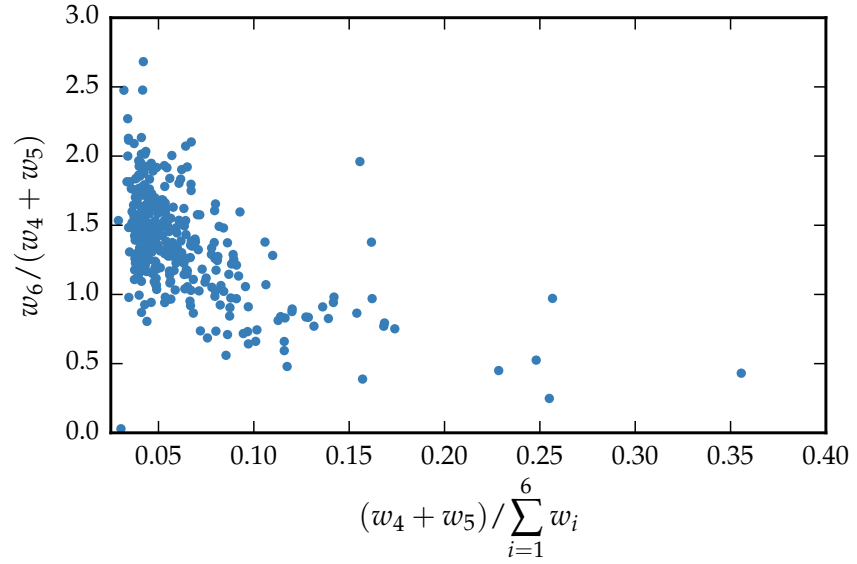


Figure 1.18: Weight in the [O III] wing relative to the weight in the [O III] core emission versus the strength of the core [O III] emission. The blue-asymmetry of the [O III] emission increases as the strength of the core component decreases.

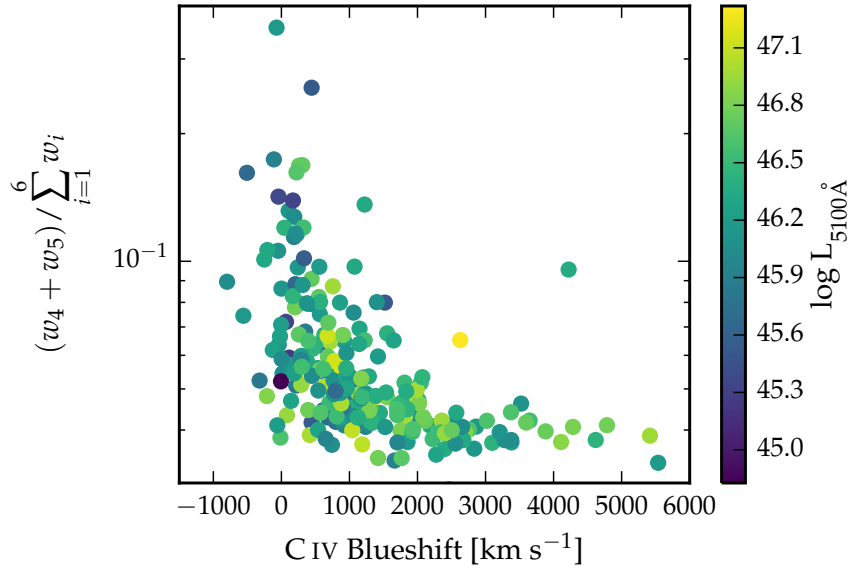


Figure 1.19: The ICA component weight w_4 , which is a proxy for the strength of core [O III], as a function of the C IV blueshift. The C IV blueshift is measured relative to the near-infrared ICA redshift.

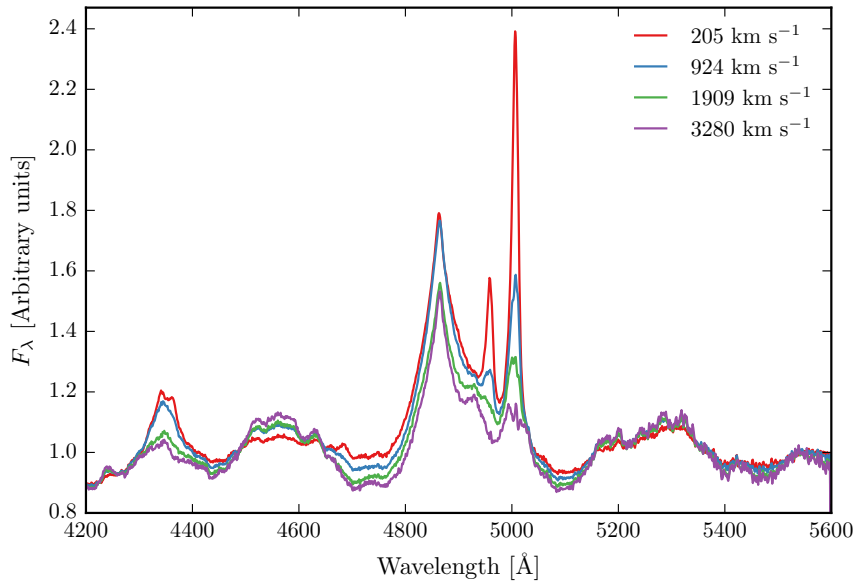


Figure 1.20: Median ICA-reconstructed spectra as a function of the C IV blueshift.

1.6.3.2 *Updating EV1*

The ICA can be thought of as update on EV1. The spectral diversity is encapsulated in the EV1 components. Most of the variance in EV1 is the anti-correlation between the strengths of [O III] and Fe II. So at one end we have objects with strong Fe II and weak [O III], and at the other end objects with weak Fe II and strong [O III]. Other properties, including the C IV blueshift and the H β FWHM, also change systematically. Our work shows that the ICA component weights change systematically along the EV1 sequence.

*Just present this as
an idea for future
work right at the end
rather than having
this sandwiched in
the middle.*

Accurate systemic redshift estimates are essential in a number of applications, and researchers have devoted a large amount of telescope time to obtaining near-infrared spectra to access [O III] for this purpose. HI, CO and absorption line measures of the host galaxy rest frame suggest that [O III] usually gives consistent results within 200 km s^{-1} (de Robertis 1985; Whittle 1985; Wilson & Heckman 1985; Condon et al. 1985; Stripe 1990; Alloin et al. 1992; Evans et al. 2001). However, our work shows that at high luminosities this can result in large errors (profile can be dominated by blueshifted component, Fe II emission can be improperly subtracted, or [O III] might not be detected at all).

The size of the narrow line region is roughly expected to scale as $L^{0.5}$ (e.g. Netzer et al., 2004). However, for high luminosity quasars with strong [O III] this gives NLR sizes which are unreasonably large ($\sim 100 \text{ kpc}$; Netzer et al., 2004).

See extra text from Brotherton paper. I could be confused here, but I think the Netzer argument goes that the nlr size increase with luminosity because there are more ionising photons. but then you run out of nlr to ionise. the luminosity of the quasar keeps increasing but the luminosity of the nlr flattens out. so the eqw starts to decrease. but we see a huge scatter in eqw at high luminosities. we can relate this to the C IV blueshift, which I don't think Netzer will have been able to.